

Shell-structure effects on high-pressure Rankine-Hugoniot shock adiabats

J.C. Pain*

October 29, 2018

Abstract

Rankine-Hugoniot shock adiabats are calculated in the pressure range 1 Mbar-10 Gbar with two atomic-structure models: the atom in a spherical cell and the atom in a jellium of charges. These quantum self-consistent-field models include shell effects, which have a strong impact on pressure and shock velocity along the shock adiabat. Comparisons with experimental data are presented and quantum effects are interpreted in terms of electronic specific heat. A simple analytical estimate for the maximum compression is proposed, depending on initial density, atomic weight and atomic number.

1 Introduction

The study of radiative properties of high-energy-density plasmas has many applications in inertial confinement fusion and astrophysics. It requires knowledge of the plasma properties in extreme conditions of density and temperature. For example, the pressure in the center of Jupiter is believed to reach 100 Mbar and temperature 25 kK, while in the center of white dwarfs pressure can exceed Gbars at temperatures of 10^7 K. In the laboratory, laser-based shock-wave experiments attain pressures of hundreds of megabars, obtained via the absorption of an intense laser pulse. The thermodynamics and the hydrodynamics of hot dense plasmas can not be predicted without a knowledge of the equation of state (EOS) that describes how a material reacts to pressure. For instance, the theory of stellar evolution is affected by uncertainties in EOS. After being predicted, brown dwarfs have recently been observed. Their internal structure and cooling time depend on the details of the EOS at densities approaching solid density and at temperatures of a few eV, conditions obtainable in laser experiments [1]. Therefore, the need for suitable EOS of high-energy-density matter becomes crucial.

*CEA/DIF, B.P. 12, 91680 Bruyères-Le-Châtel Cedex, France, email: jean-christophe.pain@cea.fr

A material subjected to a strong shock wave is compressed, heated and ionized. As the strength of the shock is varied for a fixed initial state, the ensemble of the pressure-density final states of the material behind the shock, named shock adiabat or Rankine-Hugoniot (RH) curve, depends on the EOS of the matter, which must be determined from theory. At intermediate shock pressures, when the material becomes partially ionized, the EOS depends on the precise quantum-mechanical state of the matter, *i.e.* on the electronic shell structure. Therefore, for the past twenty years there is a great interest in the physics of bound levels in high-energy-density plasmas and quantum self-consistent-field (QSCF) models [2] are replacing the older Thomas-Fermi (TF) approach [3]. We present RH curves calculated using our QSCF-based EOS code, ESODE (Equation of State with Orbital Description of Electrons). The ionic contribution to the EOS is described by an ideal gas with OCP (One Component Plasma) corrections, and the cold curve (T=0 K isotherm) has been obtained in most of the cases from Augmented Plane Wave (APW) calculations [4].

ESODE has two treatments for the thermal electronic contribution to the EOS: Average atom in a Spherical Cell (ASC) or Average atom in a Jellium of Charges (AJC). In both cases, bound electrons are treated quantum-mechanically. In the ASC model, all electrons are confined within a Wigner-Seitz sphere and free electrons are described in the TF approximation. In the AJC model, bound and free-electron wavefunctions can extend outside the sphere, where the plasma is represented by a uniform electronic density (jellium) neutralized by a continuous background of positive charges, representing ions. The QSCF models (ASC and AJC) are described in Sec. 2. Shock adiabats calculated from those models are presented, analyzed and compared to traditional TF model and to published experimental data in Sec. 3. General features of RH curves, like the interpretation of shell effects in terms of specific heat, are discussed in Sec. 3 as well. An analytical estimate for the maximum compression rate is proposed in Sec. 4. Finally, the dependence of shock velocity on particle velocity is analyzed in Sec. 5.

2 The quantum self-consistent-field models

In the present work, we consider the regime identified as strongly coupled (non-ideal) plasmas, characterized by a high density and/or a low temperature. In such plasmas, ions are strongly correlated, electrons are partially degenerate, and the coupling parameter Γ , ratio of Coulomb potential energy and thermal energy, is greater than unity. The main task is to evaluate the thermal and compressional excitations of the electrons. The determination of the average electronic charge density relies usually on the Density Functional Theory (DFT), of which a well-known example is the Thomas-Fermi (TF) model [3]. It contains essential features to characterize the material

properties in extreme conditions and is expected to be most reliable at extreme conditions when the detailed influence of the electronic structure does not play any role. Despite the omission of quantum structure, TF model typically predicts electronic densities in broad agreement with detailed approaches. However, as the pressure or temperature is raised, successive shells of electrons are delocalized and the effect of such phenomena is represented only in an averaged manner by the TF model.

2.1 Atom in a Spherical Cell (ASC)

Atoms in a plasma can be represented by an average atom confined in a Wigner-Seitz (WS) sphere, whose radius r_{ws} is related to matter density. Inside the sphere, the electron density has the following form:

$$n(r) = \sum_b f_l(\epsilon_b, \mu) |\psi_b(\vec{r})|^2 + \frac{\sqrt{2}(k_B T)^{3/2}}{\pi^2} [F_{1/2}(-\bar{V}(r), \bar{\mu} - \bar{V}(r), \chi) + \chi F_{3/2}(-\bar{V}(r), \bar{\mu} - \bar{V}(r), \chi)], \quad (1)$$

where

$$f_l(x, y) = \frac{2(2l+1)}{1 + \exp[(x-y)/k_B T]} \quad \text{and} \quad F_{n/2}(a, x, \sigma) = \int_a^\infty \frac{y^{n/2}(1 + \sigma y/2)^{1/2}}{1 + \exp[y-x]} dy \quad (2)$$

are, respectively, the Fermi-Dirac population and the modified Fermi function of order $n/2$. The first term in Eq. (1) corresponds to the contribution of bound electrons to the charge density, while the second term is the free electron contribution, written in its semi-classical TF form. The quantity ϵ_b is the energy of a bound orbital and ψ_b the associated wavefunction calculated in the Pauli approximation [5], in which only first-order relativistic corrections to the Schrödinger equation are retained. We introduce the notations $\chi = k_B T/E_0$, E_0 being the rest-mass energy of the electron and $\bar{V}(r) = V(r)/(k_B T)$, where $V(r)$ is the self-consistent potential:

$$V(r) = -\frac{Z}{r} + \int_0^{r_{ws}} \frac{n(r')}{|\vec{r} - \vec{r}'|} d^3 r' + V_{xc}[n], \quad (3)$$

V_{xc} being the exchange-correlation contribution, evaluated in the local density approximation [6]. Last, the chemical potential μ is obtained from the neutrality of the ion sphere:

$$\int_0^{r_{ws}} n(r) 4\pi r^2 dr = Z, \quad (4)$$

and $\bar{\mu} = \mu/(k_B T)$. Equations (1), (3) and (4) must be solved self-consistently provided that bound orbitals are obtained from the Schrödinger

equation at each step. The electronic pressure P_e [7] consists of three contributions, $P_e = P_b + P_f + P_{xc}$, where the bound-electron pressure P_b is evaluated using the stress-tensor formula

$$P_b = \sum_b \frac{f(\epsilon_b, \mu)}{8\pi r_{ws}^2 (1 + \frac{\epsilon_b}{2E_0})} \left[\left(\frac{dy_b}{dr} \Big|_{r_{ws}} \right)^2 + \left(2\epsilon_b \left(1 + \frac{\epsilon_b}{2E_0} \right) - \frac{1+l+l^2}{r_{ws}^2} \right) y_b^2(r_{ws}) \right], \quad (5)$$

y_b representing the radial part of the wavefunction ψ_b multiplied by r . The free-electron pressure P_f reads

$$P_f = \frac{2\sqrt{2}}{3\pi^2} (k_B T)^{5/2} [F_{3/2}(-\bar{V}(r_{ws}), \bar{\mu} - \bar{V}(r_{ws}), \chi) + \frac{\chi}{2} F_{5/2}(-\bar{V}(r_{ws}), \bar{\mu} - \bar{V}(r_{ws}), \chi)] \quad (6)$$

and P_{xc} is the exchange-correlation pressure evaluated in the local density approximation [6]. The choice of the boundary conditions plays a major role in the expression of pressure due to the fact that the energy of an orbital depends on the value of the corresponding wavefunction at the boundary of the WS sphere. In our model, the wavefunction behaves like a decreasing exponential at the boundary. The internal energy in the AJC model is

$$E_e = \sum_i q_i \epsilon_i - \frac{1}{2} \int_0^{r_{ws}} n(r) \int_0^{r_{ws}} \frac{n(r')}{|\vec{r} - \vec{r}'|} d^3r d^3r' + E_{xc} - \int_0^{r_{ws}} n(r) V_{xc}(n(r)) d^3r, \quad (7)$$

where E_{xc} is the exchange-correlation internal energy and q_i the population of state i (either bound or free). The first term in Eq. (7) can be expressed by

$$\sum_i q_i \epsilon_i = \sum_b f_l(\epsilon_b, \mu) \epsilon_b + E_{f,k} + E_{f,p}. \quad (8)$$

$E_{f,p}$ is the potential energy

$$E_{f,p} = \frac{\sqrt{2}(k_B T)^{3/2}}{\pi^2} \int_0^{r_{ws}} [F_{1/2}(-\bar{V}(r), \bar{\mu} - \bar{V}(r), \chi) + \chi F_{3/2}(-\bar{V}(r), \bar{\mu} - \bar{V}(r), \chi)] \bar{V}(r) d^3r \quad (9)$$

and $E_{f,k}$ the kinetic energy

$$E_{f,k} = \frac{\sqrt{2}(k_B T)^{5/2}}{\pi^2} \int_0^{r_{ws}} [F_{3/2}(-\bar{V}(r), \bar{\mu} - \bar{V}(r), \chi) + \chi F_{5/2}(-\bar{V}(r), \bar{\mu} - \bar{V}(r), \chi)] d^3r. \quad (10)$$

Here only non-relativistic calculations are performed, which correspond to $E_0 \rightarrow \infty$ in Eqs. (1), (5) and (6), to make comparisons with the non-relativistic model described in Sec. 2.2. Equations (1) to (10) enable one to include relativistic effects without solving Dirac equation.

2.2 Atom in a Jellium of Charges (AJC)

In order to go beyond the TF approximate treatment of continuum electron charge density, it is necessary to use a full quantum-mechanical description of the continuum states and to consider that both bound and free orbitals can extend outside the WS sphere, which requires the definition of the environment beyond the central average ion. One way to address this is the jellium model (or electron-gas model), *i.e.* a uniform electron density ($-\bar{n}_+$) neutralized by a positive background \bar{n}_+ simulating the ionic charges. The model relies on a method proposed by Friedel [8, 9] to treat the electronic structure of an impurity, represented by a spherical potential of finite range, in an electron gas. It has been further developed by Dagens [10, 11] and Perrot [12, 13, 14]. The problem is reduced to the response of the electronic density to the immersion of a positive charge Z into the jellium. These considerations lead to the following form of the electron density:

$$n(r) = \sum_b f_l(\epsilon_b, \mu) |\psi_b(\vec{r})|^2 + \sum_l \int_0^\infty f_l(\epsilon, \mu) |\psi_{\epsilon,l}(\vec{r})|^2 d\epsilon \quad (11)$$

with

$$V(r) = -\frac{Z}{r} + \int_0^{R_\infty} \frac{n(r')}{|\vec{r} - \vec{r}'|} d^3r' + V_{xc}(r) - V_{xc}(-\bar{n}_+), \quad (12)$$

where $R_\infty \gg r_a$, r_a being the radius of the cavity. The potential $V(r)$ is determined, as in the ASC model, in a self-consistent way. The ionic density is modeled by

$$n_+(r) = \begin{cases} 0 & \text{for } r < r_a \\ \bar{n}_+ & \text{for } r > r_a. \end{cases} \quad (13)$$

The expression of internal energy is [14]

$$E[n, n_+] = Z^*[e_k + e_{xc}](-\bar{n}_+) + \Delta E[n, n_+] - \Lambda_T P_1 v_a \quad (14)$$

with

$$v_a = \frac{4}{3}\pi r_a^3, \quad \Lambda_T = \left. \frac{\partial \ln Z^*}{\partial \ln T} \right|_{v_a, T} \quad \text{and} \quad P_1 = \frac{\bar{n}_+}{v_a} \int_{r_a}^{R_\infty} 4\pi r^2 V(r) dr. \quad (15)$$

Quantities e_k and e_{xc} are the kinetic and exchange-correlation energies per free electron and $\Delta E[n, n_+]$ is the immersion energy, *i.e.* the energy change resulting from the immersion of an ion in the jellium:

$$\begin{aligned} \Delta E[n, n_+] &= \int_0^{R_\infty} (e_k[n(r)] - e_k[-\bar{n}_+])d^3r - \int_0^{R_\infty} \frac{Z}{r}(n(r) + n_+(r))d^3r \\ &\quad + \frac{1}{2} \int_0^{R_\infty} \int_0^{R_\infty} \frac{n(r) + n_+(r)}{|\vec{r} - \vec{r}'|} (n(r') + n_+(r'))d^3r d^3r' \\ &\quad + \int_0^{R_\infty} (e_{xc}(n(r)) - e_{xc}(-\bar{n}_+))d^3r. \end{aligned} \quad (16)$$

The pressure is obtained by

$$P_e = [P_k + P_{xc}](-\bar{n}_+) + \bar{n}_+ U(r_a) + (1 - \Lambda_{v_a})P_1, \quad \text{where } \Lambda_{v_a} = \left. \frac{\partial \ln Z^*}{\partial \ln v} \right|_{v_a, T}, \quad (17)$$

and

$$U(r) = -\frac{Z}{r} + \frac{1}{r} \int_0^r 4\pi r'^2 (n(r') + n_+(r'))dr' + \int_r^{R_\infty} 4\pi r' (n(r') + n_+(r'))dr'. \quad (18)$$

The term P_k is the pressure of a free-electron gas. The pressure in Eq. (17) is rigorously the derivative of energy with respect to volume. This is the main difference with Liberman's model [15, 2]. The major difficulty with these models is that the average ionization is not well defined when the outer electrons are delocalized. The only way to make the formalism variational is to specify the ionization in the AJC model. In other words, the question is how to define the residual electron density $(-\bar{n}_+)$ far away from the point where the positive charge is introduced into the jellium. A convenient choice is [14] $Z^*(v) = Z_{TF}^*(v)$, Z_{TF}^* being the TF ionization. Then derivatives of ionization with respect to volume and temperature can be obtained analytically, using the numerical fit proposed by More [16]. At first sight, ASC and AJC models seem to be very different concerning the modeling of the environment of the atom, isolated and confined in the ASC model, and immersed in an infinite effective medium in the AJC model. However, when the electronic structure is calculated in the TF approximation, these models are equivalent if the jellium density $(-\bar{n}_+)$ is equal to TF density evaluated at the WS radius. Such a property comes from a variational principle (minimization of the free energy).

2.3 Ionic contribution and cold curve

The adiabatic approximation is used to separate the thermodynamic functions into electronic and ionic components. The total pressure can be writ-

ten:

$$P(\rho, T) = P_c(\rho) + P_i(\rho, T) + P_t(\rho, T), \quad (19)$$

where $P_t(\rho, T) = P_e(\rho, T) - P_e(\rho, 0)$, is the thermal electronic contribution to the EOS. The quantity P_i is the ionic pressure and subscript “c” characterizes the cold curve obtained from APW [4] simulations or using the Vinet [17] universal EOS. Equation (19) also holds for internal energy. In order to take into account non-ideality corrections to the thermal motion of ions we use an approximation [18] based on the calculation of the EOS of a One-Component Plasma (OCP) by the Monte Carlo method [19]. The ion contribution can be obtained using a formula based on the Virial theorem:

$$P_i(\rho, T) = \rho k_B T + \frac{\rho}{3} \Delta E_i(\rho, T), \quad (20)$$

where

$$\Delta E_i(\rho, T) = k_B T \left[\Gamma^{3/2} \sum_{i=1}^4 \frac{a_i}{(b_i + \Gamma)^{i/2}} - a_1 \Gamma \right] \quad (21)$$

and $E_i(\rho, T) = 3k_B T/2 + \Delta E_i(\rho, T)$ with $a_1 = -0.895929$, $a_2 = 0.11340656$, $a_3 = -0.90872827$, $a_4 = 0.11614773$, $b_1 = 4.666486$, $b_2 = 13.675411$, $b_3 = 1.8905603$ and $b_4 = 1.0277554$. Such corrections lead to small differences in the RH curves as shown in Sec. 5.

3 Rankine-Hugoniot shock adiabats

3.1 Definitions and numerical investigations

The initial state of the plasma is characterized by a density ρ_0 , a temperature T_0 , a pressure P_0 , and an internal energy E_0 . D is the shock velocity, u the matter velocity, P and E are respectively the pressure and internal energy behind the shock front. These variables obey the following Rankine-Hugoniot relation [20]:

$$\frac{1}{2}(P + P_0) \left(\frac{1}{\rho_0} - \frac{1}{\rho} \right) = E - E_0, \quad (22)$$

The RH curve can be obtained by solving Eq. (22) at each temperature step. Calculations have been performed for $T \leq 6.4$ keV for beryllium (Be, Z=4), aluminum (Al, Z=13), iron (Fe, Z=26) and copper (Cu, Z=29) calculated from pure Thomas-Fermi EOS, ASC model, and AJC model. The cold curve has been calculated using Vinet universal EOS [17] for Be and APW [4] method for Al, Fe and Cu. Results from the QSCF models differ strongly from the TF approximation and slightly from each other. In the case of Al, which we use as an example (see Fig. 1), the difference between

the theories appears for $P \geq 3$ Mbar and AJC gives higher pressures than the other models for $2 \leq \eta \leq 3.5$, where $\eta = \rho/\rho_0$ is the compression rate. For $\eta \geq 3.5$, all QSCF models give lower pressures than TF model.

3.2 Quantum orbital effects

Our models emphasize the thermodynamic domain where RH curves strongly depend on the electronic structure, *i.e.* beyond four times solid density where the shoulders (double in the case of Al, Fig. 1) correspond to ionization of successive shells. These shoulders can be explained by the competition between the release of internal energy stored in the shells and the free-electron pressure. When ionization begins, the energy of the shock depopulates the relevant shells and the material is very compressive. However, the pressure due to the free electrons eventually dominates and the material becomes less compressive. Both models show compression maxima in the range $5\rho_0 - 6\rho_0$. In this region, the electrons from the ionic cores are being ionized. The shock density increases beyond the infinite pressure of $4\rho_0$ in the electron ionization region. As ionization is completed, the plasma approaches an ideal gas of nuclei and electrons and the density approaches the fourfold density $4\rho_0$. For Be, all the models yield a single density maximum, corresponding to the ionization of the K electron shell. For Al (Fig. 1), there are two density maxima corresponding to the K and L electron shells, each followed by density decreases. For Fe and Cu there are density maxima or inflexions corresponding to the K, L and M electron shells. The L-shell ionization feature gives the largest density increase. In the case of Cu, the ASC model exhibits a kind of discontinuity around 40 g/cm^3 , due to pressure ionization of $2p$ orbital. Such a sharp increase of pressure does not exist in the AJC model, because this model is consistent from the thermodynamic point of view. This is due to the fact that the pressure is rigorously obtained as a derivative of the free energy, and shape resonances are carefully taken into account in the quantum treatment of free electrons. Such features lead to a continuous disappearing of a bound state into the continuum, which is a suitable treatment of pressure ionization. In fact, the non-monotonic character of thermodynamic variables stems from the eigen-energies of the orbitals themselves, which exhibit the oscillations as well. The first density for which decompression occurs is named “turnaround” point. The pressure differences from the quantum mechanical theory can be explained by examining the electronic heat capacity per particle predicted by the two theories along the RH path. At low temperature, the electronic heat capacity depends on the number of electrons that can be excited around the Fermi energy and the TF theory predicts a smooth increase since the density of states in this model is a monotonic function of energy. Therefore, the electronic specific heat per particle

$$\tilde{C}_v^{el} = \frac{C_v^{el}}{3k_B/2} \quad \text{where} \quad C_v^{el} = \frac{\partial[E(\rho, T) - E_i(\rho, T)]}{\partial T} \quad (23)$$

displays the signature of the ionization of successive shells. Figure 2 represents \tilde{C}_v^{el} along the RH curve in the TF and in the ASC models for Al. Both theories show the effect of the coulomb attractive potential of the nucleus binding the electrons, represented by the peak around 300 eV for TF theory and 100 eV for ASC model. After the first reduction in density on the RH curve, there are 11 free electrons and 2 bound electrons remaining in the $1s$ orbital (K shell), which is far away from the energy zero (1.5 keV at 100 eV). As long as temperature is not sufficient to ionize those two electrons, the specific heat tends to an asymptote corresponding to an ideal gas of 11 independent particles. When both $1s$ electrons are ionized (after a “threshold” temperature), there is a sudden break in the specific heat, which tends to an ideal gas of 13 independent particles. This phenomenon is a kind of “Schottky anomaly”, *i.e.* an enhancement in the specific heat (see Fig. 2). This effect is not as important for the $2s$ and $2p$ bound states (L shell), since their energy levels are not as far from the continuum (a few tenth of eV). We note that the same phenomenon occurs for Fe; in that case, after two “Schottky anomalies”, the electronic part of the specific heat tends to an ideal gas of 26 electrons.

3.3 Comparisons with experimental data

Experimental data concerning Be, Al, Fe and Cu [21] have been collected for comparison with the EOS models presented. Several experimental methods have been used to generate well-defined shock states: gas guns for pressures up to 5 Mbar, explosive-driven spherical implosions, laser-driven plane waves for generating shocks up to 10 Mbar, and through underground nuclear explosions where pressures of a few Gbar can be attained. Superimposing these data should yield a single smooth RH curve. The maximum pressures reached in the experiments are: 18 Mbar for Be, 4000 Mbar for Al, 191 Mbar for Fe and 204 Mbar for Cu. It is clear that there is difficulty discriminating between models, since there are very few available data for the region of interest, *i.e.*, above 100 Mbar). The error bars associated with the highest pressures for Al are too large to provide insight into the existence of shell effects. Analysis of the computational results shows that the deviation from the experimental points of Al can not be explained only by shell effects. In the region where most of the experimental points are available, the role of the cold component is important, while shell effects begin to play a significant role after the matter is compressed, which occurs near the limiting compression $\eta \approx 4$, and heating begins. For Fe and Cu, results from AJC model are found to be in better agreement with experimental points than the hybrid model ASC. Finally, we note that it is very difficult to relate gas

gun measurements with a discussion of shell effects as the pressures are too low to exhibit these effect.

4 Evaluation of maximum compression

The maximum compression rate depends on the choice of the boundary conditions of the wavefunctions described in Sec. 2.1. Furthermore, it depends on the calculation of the ionic part: ideal gas (IG) with or without OCP corrections (Eqs. (20-21)). For instance, the maximum rate for Al in the ASC model with IG is 4.901 and with IG and OCP corrections 4.931. OCP corrections systematically increase the maximum compression rate. As can be checked in Fig. 1 the maximum compression attainable by a single shock is larger than 4 and occurs at finite pressure. This phenomenon is due to the draining of internal energy in internal degrees of freedom, *via* ionization. An analytical expression for the maximum compression attainable by a single shock in any material from any initial state, except those with gaseous densities, can be formulated. The total energy can be written as the sum of kinetic and potential energies E_k and E_p . Neglecting exchange-correlation contribution, the virial theorem enables one to relate pressure, kinetic energy and potential energy $3P/\rho = 2E_k + E_p$. The compression rate $\eta = \rho/\rho_0$ for the standard RH curve, $P_0 = 0$, ρ_0 solid density and $T_0=300$ K, can be written

$$\eta = 4 + \frac{3}{1 + 2\frac{\delta E_k}{\delta E_p}} \quad \text{with } \delta E_k = E_k - E_{k_0} \quad \text{and } \delta E_p = E_p - E_{p_0}. \quad (24)$$

At high compression, assuming that $E_k \gg E_{k_0}$ and that all the electrons have been ionized and have a kinetic energy equal to the Fermi energy, one can write:

$$\delta E_k = Z \frac{1}{2} (3\pi^2 Z \rho \frac{N_A}{A})^{2/3} a_0^2, \quad (25)$$

where $a_0=52.9177208319 \cdot 10^{-10}$ cm is the Bohr radius, ρ is in g/cm³, and A in g. Next, at high compression the excess potential energy can be estimated as the Coulomb interaction energy of two ionic spheres

$$\delta E_p = \frac{1}{2} \frac{Z^2}{r_{ws}} \quad \text{and } r_{ws} = \left[\frac{3A}{4\pi N_A a_0^3} \right]^{1/3} \rho^{-1/3}, \quad (26)$$

where r_{ws} is the WS radius equal to the cavity radius r_a and we set $4\pi\epsilon_0 = 1$. Therefore, using Eqs. (25) and (26), which are relevant for a strongly coupled gas of degenerate electrons, the maximum compression rate η_m obeys

$$\eta_m = 4 + \frac{3}{1 + \zeta(\rho_0, Z, A)\eta_m^{1/3}}, \quad (27)$$

with

$$\zeta(\rho_0, Z, A) = 3\pi(2N_A)^{1/3}a_0\left(\frac{\rho_0}{ZA}\right)^{1/3}. \quad (28)$$

The solution is:

$$\eta_m = \left[\frac{-1 - (-1)^{\theta(\zeta - \zeta_c)} 2\zeta \sqrt{h(\zeta)}}{4\zeta} + \frac{1}{2} \sqrt{\frac{3}{4\zeta^2} - h(\zeta) - (-1)^{\theta(\zeta - \zeta_c)} \frac{32\zeta^3 - 1}{4\zeta^3 \sqrt{h(\zeta)}}} \right]^3 \quad (29)$$

where $\zeta_c = 0.314980262473$, θ is Heaviside function,

$$h(\zeta) = \frac{1}{4\zeta^2} - \frac{2^{10/3}}{\Delta^{1/3}(\zeta)} + \frac{\Delta^{1/3}(\zeta)}{2^{1/3}\zeta}, \quad (30)$$

and $\Delta(\zeta) = -7 + 16\zeta^3 + \sqrt{49 + 1824\zeta^3 + 256\zeta^6}$. Figure 3 confirms the fact that the maximum compression is always smaller than 7 [22], and strongly dependent on the density ρ_0 . Note that Eq. (29) can not be applied for gaseous ambient elements. Neglecting cohesive and dissociation energies, and using fits for the total ionization energies, Johnson [22] has proposed an analytical formula for the maximum compression rate. It seems difficult, however, to discriminate between his approach and ours with the values displayed in Fig. 3 and calculated with our QSCF models, since the disparity of values is as large as the difference between the two models. However, the present calculation does not rely on a particular form of the EOS, as in Ref. [22]. On the contrary, here the maximum compression predicted by our model is higher for Fe than for Al, which is consistent with the results presented in Ref. [2]. However, in Ref. [2] the maximum compression seems to increase with Z ; according to Johnson's model and ours, this is not true *stricto sensu* but is only a global trend.

5 Shock and particle velocities

The particle velocity and shock velocity are:

$$u = \sqrt{\frac{(\rho - \rho_0)(P - P_0)}{\rho_0\rho}} \quad \text{and} \quad D = \sqrt{\frac{\rho(P - P_0)}{\rho_0(\rho - \rho_0)}}, \quad (31)$$

Expressions in Eq. (31) are generic as they do not involve, *a priori*, any explicit relation $D(u)$. For metals, it is often assumed that the relation is quasi-linear. However, we find that the (D, u) relationship is almost linear

over a wide range of densities, except near $u = 0$ where we could not perform the calculation. It is easy to check from expressions in Eq. (31) that the slope should be $\sim 4/3$, corresponding to the ideal gas. However, when looking carefully at the first and second derivatives of shock velocity versus particle velocity, one finds that the behaviour of shock velocity is more complicated, and that there are some oscillations, reflecting the shell structure as well, and inflexions points. Deviations from linearity, indicated by curvature, are more obvious when one investigates the relationship $(D - u)$ versus u , which is illustrated in Fig. 4. The amplitude of the oscillations in the (D, u) relationship is very small, which is not the case of (P, ρ) relationship.

6 Conclusion

Shock waves generating finite-temperature dense matter make possible the generation in laboratory experiments of extremely high energy densities typical of matter in the few first microseconds after the creation of the universe and for such astrophysical objects as stars and giant planets. The physical information obtained from these experiments extends the basic knowledge of physical properties of these systems to pressures nine orders of magnitude higher than found, *e.g.*, in our atmosphere. We proposed a qualitative and quantitative study of quantum orbital effects on the principal shock adiabat for different elements, for two quantum self-consistent-field models: the atom in a spherical cell (ASC) and the atom in a jellium of charges (AJC). Quantum orbital effects lead to oscillations corresponding to the ionization of successive orbitals that are also visible in the electronic specific heat, and in the energies of the orbitals. The AJC model provides a better treatment of pressure ionization, since it relies on a full quantum treatment of the electrons. An estimate of the maximum compression, giving realistic values, has been proposed.

The next step will be to test whether the oscillations still exist “beyond” the Average Atom model, *i.e.*, when a variety of electronic configurations is taken into account [7]. It remains a difficulty in the existing models to represent, in a simple and suitable way, the influence of the plasma environment on a specific ion. Indeed, as this environment fluctuates, the number, the localization in space and the structure of neighboring ions will change drastically. Therefore we will in the future represent the ionic environment including radial distribution functions, thereby going beyond the adiabatic approximation.

References

- [1] B.A. Remington, D. Arnett, R.P. Drake, H. Takabe, *Science* **284**, 1488 (1999)

- [2] B.F. Rozsnyai, J.R. Albritton, D.A. Young, V.N. Sonnad, D.A. Liberman, *Phys. Lett. A* **291**, 226 (2001)
- [3] R.P. Feynman, N. Metropolis, E. Teller, *Phys. Rev.* **75**, 1561 (1949)
- [4] T.L. Loucks, *Augmented Plane Wave Method: A Guide to Performing Electronic Structure Calculations* (W.A. Benjamin, Inc., New York, 1967)
- [5] H.A. Bethe, E.E. Salpeter, *Quantum Mechanics of One- and Two-electron Atoms* (Springer Verlag, Berlin, 1957)
- [6] H. Iyetomi, S. Ichimaru, *Phys. Rev. A* **34**, 433 (1986)
- [7] J.C. Pain, G. Dejonghe, T. Blenski, *J. Quant. Spectrosc. Radiat. Transfer* **99**, 451 (2006)
- [8] J. Friedel, *Philos. Mag.* **43**, 153 (1952)
- [9] J. Friedel, *Adv. Phys.* **3**, 446 (1954)
- [10] L. Dagens, *J. Phys. C* **5**, 2333 (1972)
- [11] L. Dagens, *J. Phys. (Paris)* **34**, 879 (1973)
- [12] F. Perrot, *Phys. Rev. A* **42**, 4871 (1990)
- [13] F. Perrot, *Phys. Rev. A* **47**, 570 (1993)
- [14] F. Perrot, Recherche d'un modèle de structure électronique des plasmas applicable aux calculs d'opacité et d'équation d'état, unpublished
- [15] D.A. Liberman, *Phys. Rev. B* **20**, 4981 (1979)
- [16] R.M. More, Atomic Physics in Inertial Confinement Fusion, UCRL Report 84991, 5/3/1981
- [17] P. Vinet, J.H. Rose, J. Ferrante, J.R. Smith, *J. Phys.: Condens. Matter* **1**, 1941 (1989)
- [18] A.F. Nikiforov, V.G. Novikov and V.B. Uvarov, *Teplofiz. Vys. Temp.* **25**, 12 (1987)
- [19] J.P. Hansen, *Phys. Rev. A* **8**, 3096 (1973)
- [20] Ya.B. Zel'dovich, Yu.P. Raizer, *Physics of Shock Waves and High-Temperature Hydrodynamic Phenomena*, Vol. 1, Academic Press, New York, 1966, Ch. 3
- [21] A.V. Bushman, I.V. Lomonosov, K.V. Khishchenko, *Shock Wave Database* and references therein (<http://teos.ficp.ac.ru/rusbank/>)
- [22] J.D. Johnson, *Phys. Rev. E* **59**, 3727 (1999)

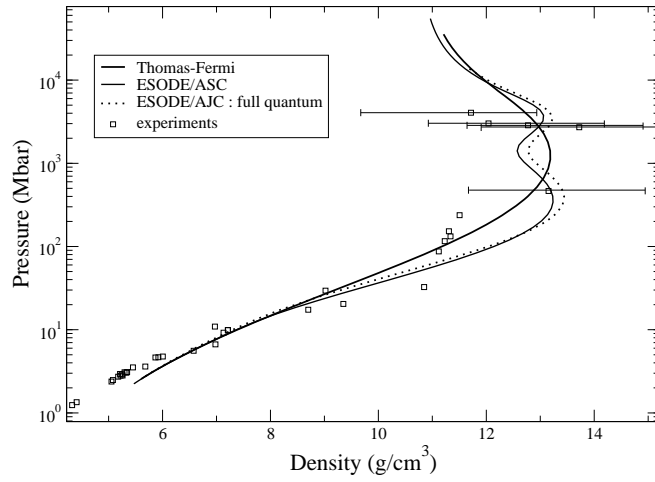


Figure 1: Rankine-Hugoniot curves for Al. $\rho_0 = 2.70 \text{ g/cm}^3$.

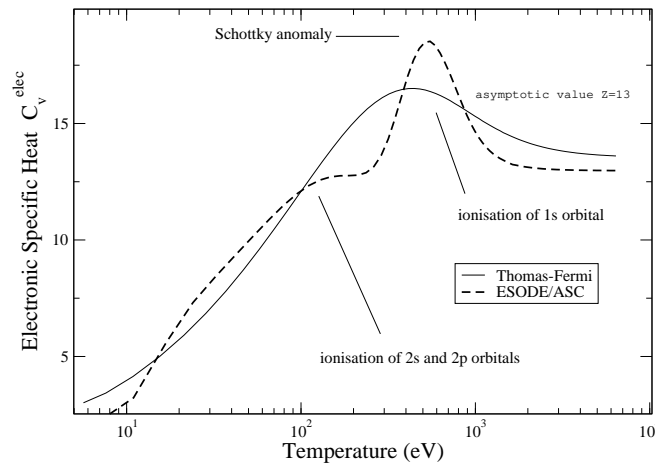


Figure 2: Electronic specific heat for Al.

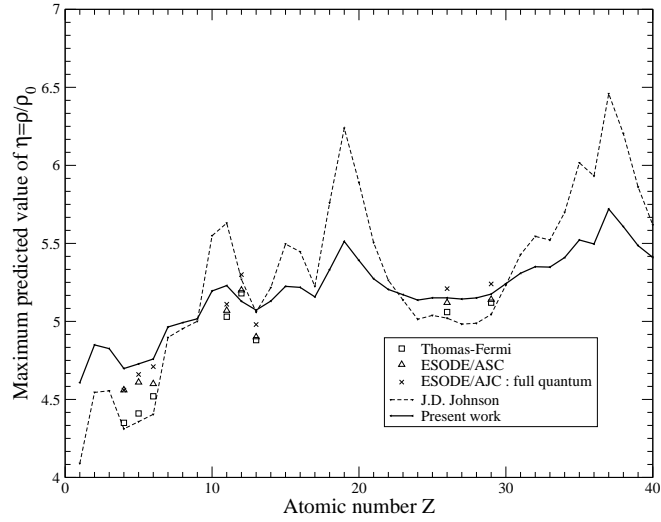


Figure 3: Maximum compression rate obtained from [22], from our model and compared to the maximum compression observed from a TF, ASC and AJC calculations for Be, B, C, Na, Mg, Al, Fe and Cu.

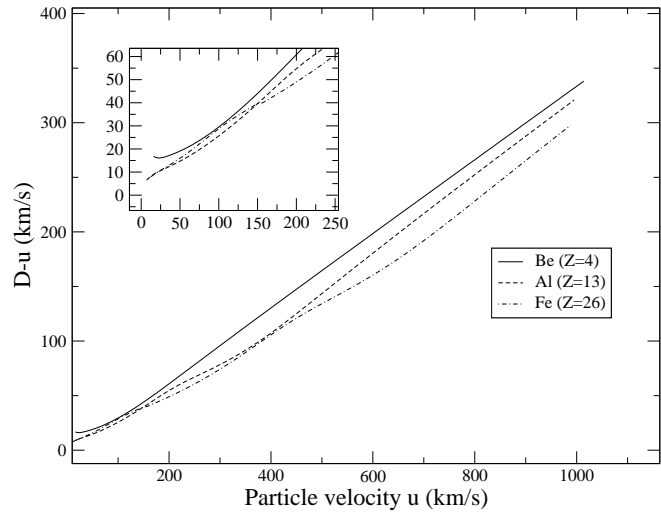


Figure 4: $(D - u)$ versus particle velocity u for Be, Al and Fe.